

# High order momentum topological insulator in 2D semi-Dirac materials

Marta García Olmos,<sup>1,2,\*</sup> Yuriko Baba,<sup>3,4,†</sup> Mario Amado,<sup>1,‡</sup> and Rafael A. Molina<sup>2,§</sup>

<sup>1</sup>*Nanotechnology Group, USAL—Nanolab, University of Salamanca  
Plaza de la Merced, Edificio Trilingüe, 37008, Salamanca, Spain.*

<sup>2</sup>*Instituto de Estructura de la Materia IEM-CSIC, Serrano 123, E-28006 Madrid, Spain*

<sup>3</sup>*Department of Theoretical Condensed Matter Physics,  
Condensed Matter Physics Center (IFIMAC) Universidad Autónoma de Madrid, E-28049 Madrid, Spain*

<sup>4</sup>*GISC, Departamento de Física de Materiales,  
Universidad Complutense, E-28040 Madrid, Spain*

Semi-Dirac materials in 2D present an anisotropic dispersion relation, linear along one direction and quadratic along the perpendicular one. This study explores the topological properties and the influence of disorder in a 2D semi-Dirac Hamiltonian. Anisotropic edge states appear only in one direction. Their topological protection can be rigorously founded on the Zak phase of the one-dimensional reduction of the semi-Dirac Hamiltonian, parametrically depending on one of the momenta. In general, only a single value of the momentum is topologically protected so these systems can be considered as high order momentum topological insulators. We explore the dependence on the disorder of the edge states and the robustness of the topological protection in these materials. We also explore the consequences of the high order topological protection in momentum space for the transport properties in a two-terminal configuration.

## I. INTRODUCTION

Condensed Matter physics has been revolutionized with the emergence of two-dimensional materials and heterostructures. These materials often exhibit unconventional behavior due to their unique band structures that deviate from the usual quadratic dispersion becoming linear around the Fermi energy. The charge carriers behave then as relativistic massless fermions and can give rise to quantized transport properties and possible protected surface states due to non-trivial topology of the bulk electronic band structure. The first and paradigmatic example of such Dirac material in 2D is graphene which is a one-atom-thick carbon sheet on a honeycomb lattice [1, 2]. Since then, the exploration of novel materials has expanded, revealing several examples with intriguing topological features such as topological insulators [3–5] and Weyl semimetals [6–8].

In contrast, semi-Dirac 2D materials display a linear dispersion along one direction and a quadratic one along the perpendicular direction of the momentum space. This dispersion has been predicted in a wide variety of materials, VO<sub>2</sub>/TiO<sub>2</sub> nanostructures [9],  $\alpha$ -(BEDT-TTF)<sub>2</sub>I<sub>3</sub> salts under pressure [10], phosphorene [11, 12], thin films of Cd<sub>3</sub>As<sub>2</sub> [13] and silicene oxide [14], among others. Uniaxial strain applied on graphene, or, in general, a monoatomic honeycomb lattice induces also a semi-Dirac dispersion [15]. Several theoretical studies have addressed the different transport, optical and magnetic properties of these types of materials [16–19].

The potential for these materials to exhibit topological properties lies in the presence or absence of band inversion [4, 20, 21]. In 2D crystalline materials the standard topological number for evaluating topological properties is the Chern number that can be computed by integrating the Berry curvature in the first Brillouin zone. A finite Chern number  $C$  implies a quantized non-zero anomalous Hall conductance proportional to  $C$  [22, 23]. However, due to their anisotropic nature, two-dimensional topological invariants cannot fully capture the topological properties of semi-Dirac materials and the Chern number for these materials is zero. [15, 17, 24]. The anisotropic band structure in the standard semi-Dirac model comes from the merging of two Dirac cones [17]. A new type-II semi-Dirac dispersion coming from the merging of three Dirac points has been proposed and applied to VO<sub>2</sub>/TiO<sub>2</sub> nanostructures. For that case, in the presence of spin-orbit coupling the Chern number obtained is  $C = -2$  [24]. In our work, we do not consider such model and concentrate on the type-I semi-Dirac model that can be derived from a strained honeycomb lattice, see for example [25, 26].

Our idea is then to reinterpret the problem in terms of one-dimensional invariants parametrically depending on the momentum of one specific spatial direction. Thus, it is possible to compute the Zak phase [21, 27], a standard one-dimensional topological number, as a function of one of the momenta of the system to study the topological properties of our model. We find that the Zak phase is non-trivial only for the zero momentum state where the eigenstates are degenerate. This is consistent with the fact that the dispersion of the edge states appearing for the type-I semi-Dirac model is quadratic and not linear and with the Chern number being zero. Although, edge states appear in one of the directions for a finite semi-Dirac nanoribbon only one single state is topologically

\* mgarcia.o@usal.es

† yuribaba@ucm.es

‡ mario.amado@usal.es

§ rafael.molina@csic.es

protected. This is comparable to the behavior of high order topological insulators [28] where the topological protection is based on a dimensional reduction of the Hamiltonian [29]. However, for the model we consider this occurs in momentum space instead of the spatial dimensions.

This fact implies that, although, we do not have anomalous quantum Hall conductance in semi-Dirac materials, we should observe an anisotropic robust quantization of the two-terminal conductance for small bias due to the topologically protected zero mode state. We have explored the interplay of topology and disorder in semi-Dirac materials by studying the properties of our model as a function of disorder, including the participation ratio of the edge states and the two-terminal conductance. We find that the states closer to zero momentum in one of the directions are more robust to disorder perturbations in consistency with the results from the topological analysis.

The paper is organized as follows. In Sec. II, we introduce the model and an analytical approach to characterize the edge states. In Sec. III we clarify the definition of the topological invariant for semi-Dirac materials and we prove that strict topological protection only applies to a zero momentum state in one direction. Then, we analyze the resilience of edge states to disorder. In Sec. IV we introduce two different models of disorder and study its effect on the expected value of the position in the direction perpendicular to the decay of the edge states and the conductance.

## II. SEMI-DIRAC MODEL

Our model represents a two-banded type-I semi-Dirac material in two-dimensions where we have included a mass term. To represent this system we consider a  $k \cdot p$  Hamiltonian, generically expressed for two bands as  $H_0(\mathbf{k}) = \vec{d}(\mathbf{k}) \cdot \vec{\sigma}$ . This Hamiltonian encapsulates the fundamental low-energy physics of our system. We do not include terms proportional to the unit matrix as they do not impact the topological properties we are interested in. Here,  $\vec{d}(\mathbf{k})$  is a vector in the momentum space, and  $\vec{\sigma}$  is a vector containing the Pauli matrices. In the semi-Dirac case, the components of the vector  $\vec{d}(\mathbf{k})$  are written in the following form

$$\vec{d}(\mathbf{k}) = \begin{pmatrix} V_x k_x^2 \\ V_y k_y^2 \\ M_0 - M_{1x} k_x^2 - M_{1y} k_y^2 \end{pmatrix}, \quad (1)$$

where all the parameters are real. The eigenvalues and eigenvectors can be expressed in terms of the  $\mathbf{d}(\mathbf{k})$ -vector generically as

$$E_{\pm} = \pm d \Psi^{\pm} = \frac{1}{\sqrt{2d(d \pm d_z)}} \begin{pmatrix} d_z \pm d \\ d_x + i d_y \end{pmatrix}, \quad (2)$$

with  $d = |\mathbf{d}(\mathbf{k})|$ .

The minimal model for semi-Dirac Hamiltonians does not include the quadratic terms with  $V_x$

and  $M_{1y}$ . However, taking into account symmetry considerations, these terms should be possible for most materials. The term with  $M_{1y}$  is essential when considering band inversion and the topological properties while the term with  $V_x$  controls the dispersion properties close to  $k_x = 0$ . The bulk band structure of the model for a case with  $M_{1x} = M_{1y} = M_1$  is displayed schematically in Fig. 1. The spectrum is gapped due to the mass term  $M_0$ . The change in the sign of the  $M_0/M_1$  ratio closes and reopens the gap, switching the bands from a regular gap to an inverted one as shown in the different panels of the figure. The dispersion relation exhibits a quadratic dependence in the  $x$ -direction of the momentum space and a linear dependence in the  $y$ -direction. This anisotropic dispersion reflects the different behaviors of charge carriers along the two directions in momentum space.

### A. Characterization of the edge states

In this section we derive analytically the edge states for a nanoribbon with finite width in  $y$ -direction and periodic boundary conditions in  $x$ -direction. For simplicity, we consider each edge separately, treating them as isolated edges of the infinite half-planes defined by  $y \geq W/2$  for the upper edge and  $y \leq -W/2$  for the lower edge. This approximation suits the regime of a nanoribbon with width  $W \gg \lambda$  being  $\lambda$  the decay length of the states. In this regime, both edges can be solved separately neglecting the hybridization generated by the finite size in  $y$ -direction.

We explore solutions that decay exponentially from the edge in the confined direction and travel as a plane-wave along the  $x$ -direction,  $\psi_{k_x}^{\pm} \sim e^{i k_x x} e^{\mp \lambda (\pm W/2 - y)} (\alpha, \beta)^T$  where the decay length satisfies  $\text{Re}(\lambda) > 0$ . The two signs refer to the two edges located at  $y = \pm W/2$  respectively,  $\alpha$ ,  $\beta$  and  $\lambda$  are complex numbers.

Solving the eigenvalue problem yields to the same expression for both edges,

$$E = \pm \sqrt{[M_0 - M_{1x} k_x^2 - M_{1y} \lambda^2]^2 + V_x^2 k_x^4 - V_y^2 \lambda^2}. \quad (3)$$

which results in four roots,  $\pm \lambda_1$  and  $\pm \lambda_2$  whose explicit expressions are included in Appendix A. Note that the  $\lambda_i$  for  $i = 1, 2$  are functions of the model parameters and they depend explicitly on the momenta  $k_x$ .

To ensure the required exponential decay positive values of  $\lambda$  describe edge states decaying from the upper edge while the negative ones describe edge states decaying from the lower edge. The solution then takes the general form,

$$\psi_{k_x}^{\pm} = A_1 \begin{pmatrix} \alpha_1 \\ \beta_1 \end{pmatrix} e^{\mp \lambda_1 (\pm W/2 - y)} + A_2 \begin{pmatrix} \alpha_2 \\ \beta_2 \end{pmatrix} e^{\mp \lambda_2 (\pm W/2 - y)}, \quad (4)$$

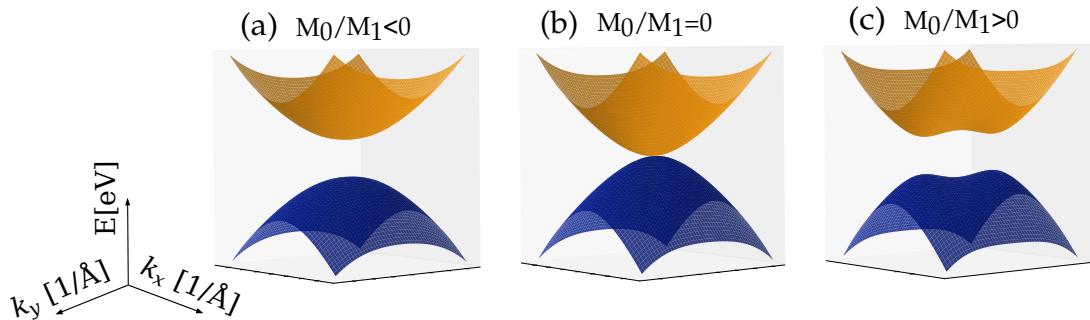


FIG. 1. Band structure of the bulk states associated to the semi-Dirac Hamiltonian (1) in terms of the  $\text{sgn}(M_0/M_1)$ . For  $M_0 = 0$  (b), the gap closes, distinguishing the transition between the trivial regime, (negative sign of  $M_0/M_1$ , (a)) and the band-inversion regime (positive sign of  $M_0/M_1$ , (c)).

where  $\alpha_i = V_x k_x^2 \mp V_y \lambda_i$  and  $\beta_i = E - M_0 + M_{1x} k_x^2 - M_{1y} \lambda_i^2$  and  $A_i$  are normalization constants.

By employing the proposed *ansatz* in the Schrödinger equation with Dirichlet boundary conditions  $\psi_{k_x}^{\pm}(y = \pm W/2) = 0$ , we obtain the dispersion relation for the edge states as a function of the decay lengths (A2),

$$E^{\pm} = M_0 - M_{1x} k_x^2 - M_{1y} (\lambda_1 \lambda_2) \mp M_{1y} \frac{V_x}{V_y} k_x (\lambda_1 + \lambda_2). \quad (5)$$

In order to clarify the dependency on the momentum  $k_x$ , it is illustrative to perform an expansion around  $k_x = 0$ . This way we obtain a quadratic dispersion in  $k_x$

$$E^{\pm} \simeq M_0 + M_{1y} (\lambda_1^{(0)} \lambda_2^{(0)}) \mp M_{1y} \frac{V_x}{V_y} (\lambda_1^{(0)} + \lambda_2^{(0)}) k_x^2. \quad (6)$$

Here,  $\lambda_i^{(0)}$  are two constants that depend only on the Hamiltonian parameters obtained by evaluating the decay lengths at  $k_x = 0$ .

There are two things that we want to highlight about these results. Firstly, non-linear dispersion and the complicated dependence of the spinor coefficients imply that the edge states are not chiral which is consistent with the value of  $C = 0$  of the Chern number. Secondly, in this two-band Hamiltonian there is a correspondence between the sign of the decay length and the sign of the energy, which are opposite. In other words, the wavefunction  $\psi^-$  corresponds to edge states decaying in the positive half-plane, i.e. for  $y > -W/2$ , and is associated with negative energy values. The opposite is true for negative values of  $\lambda$ , so the electronic or hole character of the edge states depend on whether they are in the upper or lower edge of the ribbon. The lack of chirality indicate a symmetry imbalance, in order to restore the symmetry, a  $4 \times 4$  Hamiltonian with opposite chirality would be needed. Thus, spin degrees of freedom are incorporated, allowing the inclusion of Kramer pairs similarly to the case of the quantum spin Hall models [5].

To further investigate the nature of these states,

we have relied on numerical simulations. The simulations are based on nearest-neighbor tight-binding discretization of the model described by Eq. 1 in a square lattice. To implement this, we use Kwant library [30], an open-source python-package that efficiently can be employed also for the transport calculations exposed in the following section. All figures have been made with the set of parameters included in table I, for which there is band inversion. The left panel of Fig. 2 shows the

$M_0$ [eV]	$M_{1x}$ [eV/Å <sup>2</sup> ]	$M_{1y}$ [eV/Å <sup>2</sup> ]	$V_x$ [eV/Å <sup>2</sup> ]	$V_y$ [eV/Å] (R/C)
0.09	0.23	0.23	-0.38	-0.5 / -0.18

TABLE I. Set of parameters of the model in the band inversion regime used for the figures. The two values of  $V_y$  correspond to a case with exponential decay and a case with oscillatory decay. See the text for details. We have used  $V_y = -0.5$  eV/Å except in the right panel of Fig. 4.

bands of a nanoribbon of width  $W = 66$  Å centered at  $y = 0$  and with translational symmetry in the  $x$ -direction, so  $k_x$  is a good quantum number. In the right panel we show the probability density of the edge states for  $k_x = 0.04$  Å<sup>-1</sup>, the upper edge corresponds to electronic excitations and the lower one to hole excitations. In this semi-infinite system, the edge states are degenerate for  $k_x = 0$  since the term that couples them,  $V_x k_x^2$ , disappears. The width of the gap due to finite size effects is so small for the width considered that it cannot be seen in the figure. We discuss this gap in the following paragraph. The dots in the figure correspond to the analytical expression for the dispersion of the edge states from Eq. 5. The agreement between the analytical results and the numerical simulations is excellent as the nanoribbon width is large enough to show uncoupled edges. Additionally, in Fig. 3 we present the spectrum associated with the confined states in the  $x$ -direction with the same width and with periodic boundary conditions in the  $y$ -direction, to show that there are no edge states due to the quadratic dependence in this direction.

From the previous results, we can differentiate

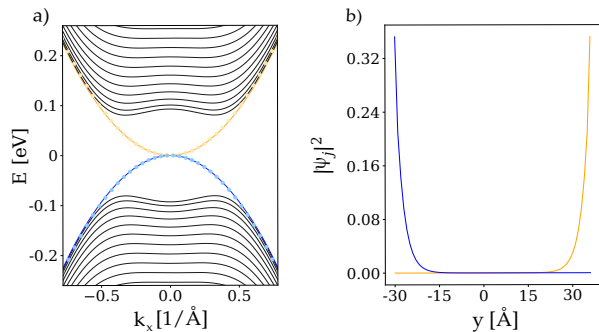


FIG. 2. Panel (a): band structure of a finite size system with translational symmetry in  $x$ -direction. The solid line corresponds to the numerical result and the dotted line is the analytical result for the edge state. Panel (b): probability density of the edge states for  $k_x = 8 \cdot 10^{-3} \text{ \AA}^{-1}$  in terms of the sites of the nanoribbon. The orange line corresponds to the edge state with positive energy,  $E = 5 \cdot 10^{-4} \text{ eV}$  and localization in the upper edge. Conversely, the state with negative energy  $E = -5 \cdot 10^{-4} \text{ eV}$  is depicted in blue and it is localized in the lower edge.

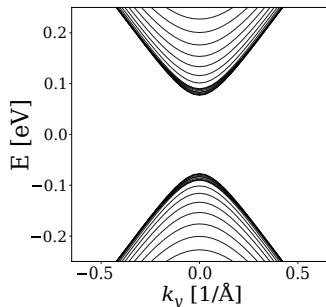


FIG. 3. Bands of a system with translational symmetry in  $y$ -direction and boundaries in  $x$ -direction.

two cases depending on the nature of the decay length of the states, if  $V_y^2 < 4M_0M_{1y}$  the decay lengths have a non-zero complex part, while for  $V_y^2 > 4M_0M_{1y}$ , they are purely real. This situation is similar in other topologically protected edge states [31].

For finite systems the real or complex nature of  $\lambda$  is going to determine how the width of the gap between edge states at  $k_x = 0$  due to finite size effects changes with the width of the system [32]. For  $\lambda$  purely real the gap has an exponential dependence with the width of the system while for complex  $\lambda$  the dependence is oscillatory. In Fig. 4 we compare the behavior of the finite size gap between the complex and the purely real values of  $\lambda$  for the two values of  $V_y$  included in table I.

### III. TOPOLOGICAL CHARACTER

In this section, we investigate the particular topological protection of the edge states appearing in our system. As previously mentioned, due to the anisotropic nature of the semi-Dirac model,

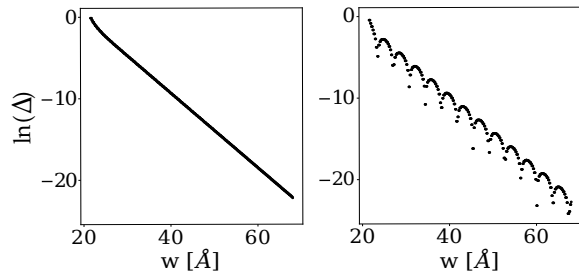


FIG. 4. Natural logarithm of the gap versus the width of the system in a nanoribbon of width  $W$  and periodic boundary conditions in the  $x$ -direction. While in the real case the gap decays exponentially, in the complex case it decays oscillatorily. The parameters used in the simulations are collected in Table I with  $V_y = -0.5 \text{ eV/ \AA}$  in the left panel and  $V_y = -0.18 \text{ eV/ \AA}$  in the right panel.

the two-dimensional invariants do not capture the topological properties. Instead, the relevant topological aspects are associated to the geometric phase acquired during the adiabatic evolution of a quantum state along a closed path in the  $k_y$ -direction, rather than in the entire Brillouin zone. This is directly linked to the Zak phase, a one-dimensional invariant that becomes a key element revealing the system's topological intricacies. For the  $n$ -band, it is defined as [27],

$$\mathcal{Z}^n = i \oint dk \langle u_n(\mathbf{k}) | \partial_k | u_n(\mathbf{k}) \rangle, \quad (7)$$

where  $|u_n(\mathbf{k})\rangle$  are eigenvectors of the bulk Hamiltonian. This quantity is well known in one-dimensional systems with inversion symmetry, where it takes two values, zero for the trivial phase and  $\pi$  for the topological phase. The most paradigmatic example is the Su-Schrieffer-Heeger model (SSH model) [33].

Treating our problem as a  $k_x$ -dependent one-dimensional model and integrate over all possible values of  $k_y$ , one can compute this topological invariant along each line of constant  $k_x$  within the Brillouin zone. The result, obtained with z2pack package [34] for a non-trivial set of values, is shown in Fig. 5 for the upper and lower band, where we compare it with the shape of the bands for a finite width nanoribbon. Focusing on the upper band, the Zak phase is maximum for  $k_x = 0$  where  $\mathcal{Z} = \pi$  and then decays continuously. The Zak phase is not quantized outside the  $k_x = 0$  and  $k_x = \pm\pi/a$  points. This lack of quantization reflects that fact that the symmetry protecting the topology at  $k_x = 0$  is not present for other values of  $k_x$  [35–37]. In Fig. 5 we can examine the correlation between the behavior of the Zak phase and the existence of edge states. For the values of  $k_x$  where the edge states mix with the bulk bands the Zak phase approaches zero. Only at  $k_x = 0$  we expect full topological protection of the edge states according to the bulk-edge correspondence.

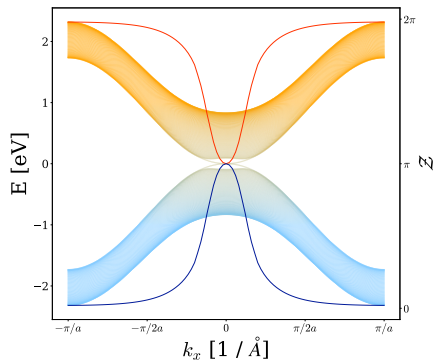


FIG. 5. Zak phase (computed in the bulk) of the system in terms of different  $k_x$  values overlapped with the band structure of a nanoribbon with finite width in the  $y$ -direction as a function of  $k_x$ .

Indeed, this zero energy state at  $k_x = 0$  can be mapped into the zero energy state of a SSH model so it is topologically protected by chiral symmetry, represented, in this case, by the  $\sigma_x$  operator [38]. To illustrate this correspondence, one can check that a discretize version (employing the substitution  $k_i \rightarrow \frac{1}{a} \sin(k_i a)$ ,  $k_i^2 \rightarrow \frac{2}{a^2} (1 - \cos(k_i a))$ ) [21] of our continuous semi-Dirac Hamiltonian with  $k_x = 0$  can be obtained by applying a rotation  $R = \exp(i\pi/4\sigma_y)$  in the Pauli matrix space around the  $\sigma_y$  axis to a generalized SSH Hamiltonian. To make this connection we consider that the Hamiltonian of the SSH model can be written as

$$H_{\text{SSH}} = [v + w_1 \cos(ka)] \sigma_x + w_2 \sin(ka) \sigma_y, \quad (8)$$

with  $v = M_0 - 2M_1/a^2$ ,  $w_1 = M_1/a^2$  and  $w_2 = V_y/a$ . In the standard SSH model  $w_1 = w_2$ , but this generalized SSH model keeps the chiral symmetry and the topological protection of the edge states. However, when  $k_x \neq 0$ , additional terms proportional to  $\sigma_z$  appear that break chiral symmetry. The Zak phase is, thus, not quantized, and the edge states are not topologically protected by symmetry. However, the closest the value of  $\mathcal{Z}$  is to  $\pi$ , the more localized are the corresponding edge states.

The situation is then similar to high order topological insulators where gapless topological protected states are localized not in the edges but in corners [28]. The difference is that in this model the topological protection affects only singular values in momentum space. We can consider this model as an example of high order momentum topological insulator in the reciprocal space.

#### IV. DISORDER SIMULATIONS

In this section we include disorder in the simulations to check the robustness of the particular topological protected zero mode in the semi-Dirac model and compare it with the other edge states with quadratic dispersion.

For our numerical simulations we employ the finite size system of length  $L = 50a$  and  $W = 66a$ .

We consider Anderson disorder, which is introduced in the Hamiltonian by adding the following onsite term,

$$H_A = \sum_i \varepsilon_i c_i^\dagger c_i. \quad (9)$$

In this case, the on-site energies  $\varepsilon_i$  are random numbers uniformly distributed in the range  $[-\frac{w}{2}, \frac{w}{2}]$  where  $w$  represents the amplitude of disorder. We present the results of an ensemble of 1500 realizations.

Chiral symmetry implies that the Hamiltonian anticommutes with a specific chiral operator, in our model  $\sigma_x$ . The eigenvalues of the Hamiltonian can be classified into pairs with opposite energy so in this context is the same as particle-hole symmetry. If  $|\Psi\rangle$  is an eigenstate with eigenvalue  $E$ , then  $\sigma_x |\Psi\rangle$  is also an eigenstate with eigenvalue  $-E$ . As chiral symmetry is so central in the topological protection of the zero mode in the semi-Dirac Hamiltonian, we want to analyze the difference in the robustness of the edge states and topological properties between a disorder breaking chiral symmetry and a disorder preserving the chiral symmetry.

Given that our system has two degrees of freedom per site, an easy way to analyze the impact of losing this symmetry is to implement the disorder in such a way that, in each realization, we can either preserve the particle-hole symmetry by including the Anderson term by

$$H(\mathbf{k}) = H_0(\mathbf{k}) + H_A(w)\sigma_z, \quad (10)$$

or by breaking the symmetry with

$$H(\mathbf{k}) = H_0(\mathbf{k}) + H_A(w)\sigma_0. \quad (11)$$

Among other things, preserving this symmetry ensures that disorder does not cause the overlap of the electron and hole states. In Fig. 6 we show the ensemble average density of states for both types of disorder and comparing also results for real and complex values of the decay length  $\lambda$ . The figure shows the effect close to  $E = 0$  of the mixing between the particle and hole sectors. When the disorder breaks the particle-hole symmetry, the dip in the DOS at zero energy is lost. Although the qualitative behavior as a function of disorder is similar for real and complex values of  $\lambda$ , the destruction of the dip is seen more clearly for complex decay lengths. One may notice that in the absence of disorder, there are more states close to zero energy for complex decay lengths than for real decay lengths as the result of parametric dependence.

To study the impact of disorder on the edge states close to the topologically protected zero mode, we perform a numerical analysis by direct diagonalization of the tight-binding Hamiltonian. The ensemble average expected value of the centroid of the density of the states in the  $y$ -direction and their participation ratio (PR) are computed as functions of the disorder magnitude. The PR is

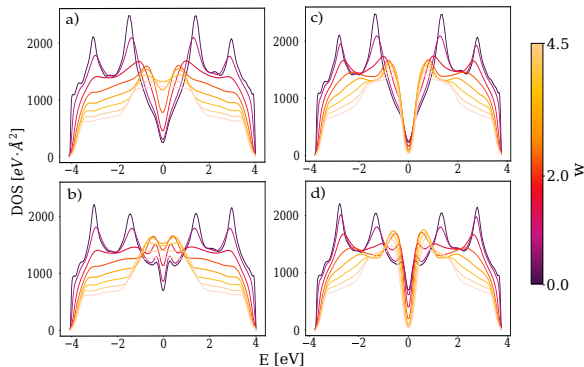


FIG. 6. Density of states for different magnitudes of the disorder for the case of disorder breaking particle-symmetry (a), real  $\lambda$ , (b), complex  $\lambda$  and for the case in which the symmetry is preserved, (c) real  $\lambda$  and (d) complex  $\lambda$ .

defined as

$$\text{PR} = \left( \sum_{i=1}^N p_i \right)^2 / \sum_{i=1}^N p_i^2, \quad (12)$$

where  $p_i = \left| \langle i | \Psi \rangle \right|^2$  and  $i$  is the site index of the tight-binding discretization. The PR provides a measure of the localization of the wave functions. A high PR suggest a uniform distribution across all sites, while a low PR indicates localization. We study the case of real and complex nature of the decay length to explore potential differences. However, for the studied value of the width where the coupling between opposite edges is almost absent and the differences are mainly the result of parametric dependence. We define the centroid of the density as

$$\langle |y| \rangle = \int_{-L/2}^{L/2} \int_{-W/2}^{W/2} |y| |\Psi(y, x)|^2 dy dx. \quad (13)$$

The results for both quantities are plotted in Fig. 7. The value of  $\langle y \rangle$  distinguishes between edge states centered close to the edge at  $y = 33a$  and bulk states with  $\langle y \rangle$  close to the center of the nanoribbon. This difference can also be observed in the value of PR. In the edge states there is a transition between edge localization and Anderson localization dominated by disorder effects that corresponds to a transition from  $\langle y \rangle$  close to the edge to  $\langle y \rangle$  inside the bulk. This transition occurs for higher values of the disorder strength  $w$  and is much more abrupt for the states closer to  $E = 0$ . This states are also more robust to perturbations due to symmetry-preserving disorder (left block) than to perturbations breaking the chiral symmetry (right block).

We also show the conductance as a function of disorder in a two-probe setup. Conductance is computed using the Landauer-Büttiker formalism [39], and averaging over disorder realizations. In Fig. 8 we show the results of the conductance as a

function of the Fermi energy of the contacts for the two different types of disorder, symmetry-breaking (left) and symmetry-preserving (right). We only show the results for the parameters given the real decay length, the case with the complex decay length being very similar. The different colors in the figure show the curves as a function of the disorder strength. We can see that conductance steps appear at integer values of  $e^2/h$ , since we are considering only one spin channel. The robustness of the first quantization step as a function of disorder it is quite remarkable, specially for the symmetry-preserving case.

For comparison, we show in Fig. 9 the conductance in the  $x$ -direction with the same parameters and values of disorder. In this case, there are no edge states contributing to the conductance at zero energy and all the transport comes from the bulk.

In Fig. 10 we plot the evolution of the averaged conductance for an energy of 0.04 eV (which is at half the first quantization step when  $w = 0$ ) as a function of the disorder for the two cases presented. In order to quantify the sensitivity to disorder of the transport properties of our system we study the value of disorder  $w_c$  at which the conductance at  $E = 0.04$  eV drops below 60% of the conductance quantum. In the case without symmetry, this quantity is  $w_c = 0.22 \pm 0.04$  while in the case with symmetry,  $w_c = 0.81 \pm 0.04$ .

## V. SUMMARY AND CONCLUSIONS

We have studied the anisotropic edge states appearing on a semi-Dirac model using a  $k \cdot p$  Hamiltonian that includes a mass and a curvature term. This special dispersion relation is halfway between the typical semiconductor spectrum, with quadratic dependence, and the Dirac spectrum, with linear dependence. As a result, when the parameters of the model present band inversion, edge states are present in the system but only in one direction.

A simple exponential *ansatz* for the description of the edge states enables us to derive their wave functions and dispersion relation. These states exhibit a quadratic dispersion and no chiral properties as a function of the momentum. Their hole or particle character depends on whether they belong to the upper or lower edges of the finite nanoribbon. These properties may suggest that the edge states have no topological character in this model and are consistent with the value of the Chern number  $C = 0$ . We have verified numerically the analytical results.

We have then explored a different strategy to understand better the topological properties of our anisotropic model and the character of the edge states. Instead of computing the 2D Chern number we have computed a one-dimensional topological number, the Zak phase, for each value of the momentum  $k_x$  in the direction of the quadratic

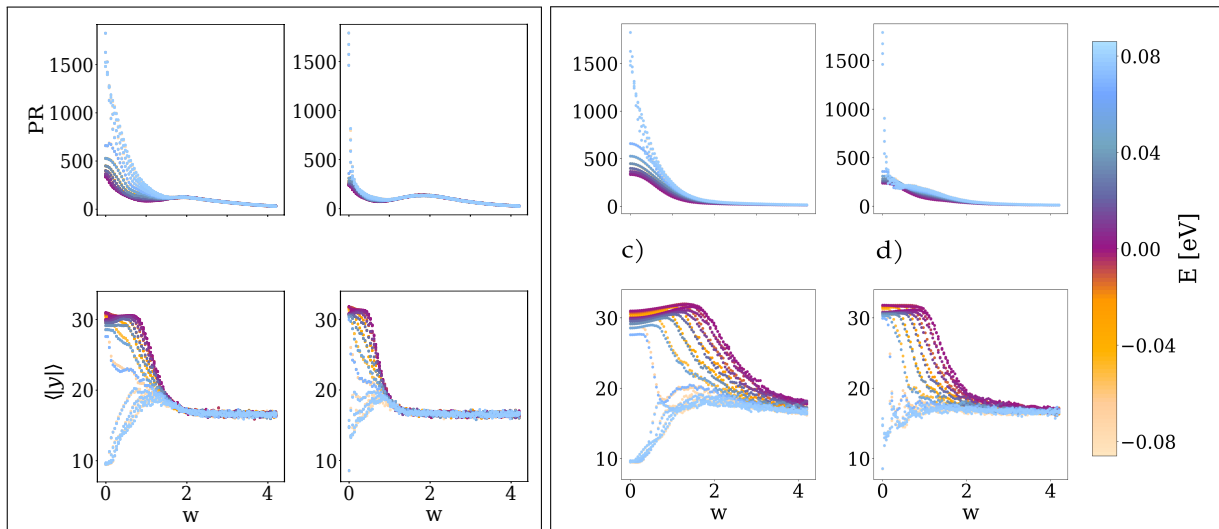


FIG. 7. Participation ratio, PR, and expected value of  $y$ -position,  $\langle y \rangle$ , in terms of the magnitude of disorder for 22 eigenstates around zero energy. The first box contains the results for the case where the disorder realizations break the p-h symmetry and the second inset shows the results when the disorder preserves this symmetry. (a) purely real decay length breaking the symmetry, (b) complex decay length breaking the symmetry, (c) purely real decay length preserving the symmetry, (d) complex decay length preserving the symmetry.

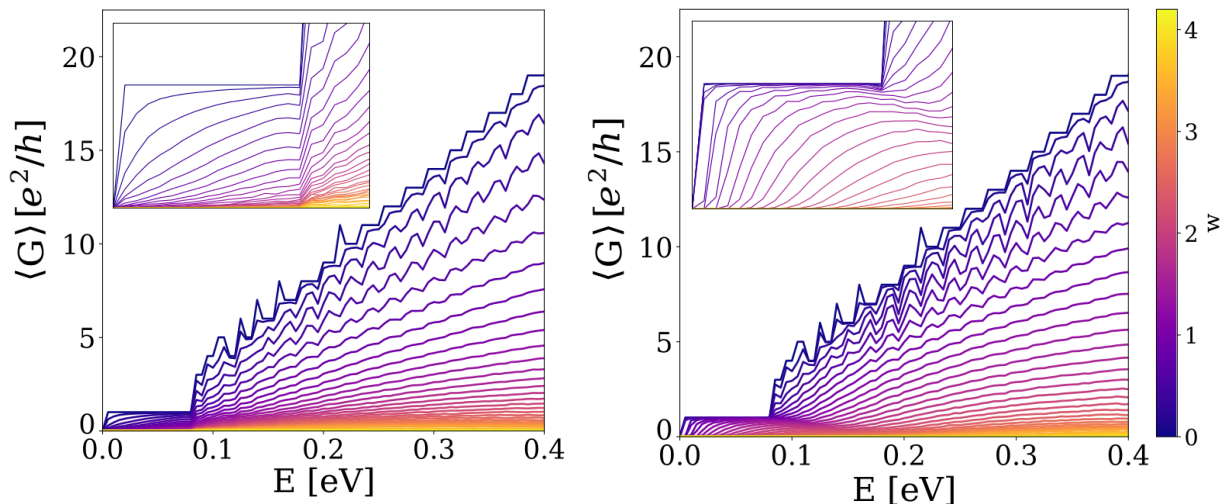


FIG. 8. Conductance averaged over 1500 realizations of disorder in terms of the energy for different magnitude of disorders. On the left is the case in which symmetry is preserved, while on the right is the case in which symmetry is broken.

dispersion. We have found a non-trivial Zak phase only for the zero mode state at  $k_x = 0$ . Only these zero modes are protected due to the chiral (or particle-hole) symmetry of the model at this point. This central result of our work is similar to the dimensionality reduction of topological properties that occur in high-order topological insulators [28]. However, instead of spatially confined topological protected states like corner states, here we have a state extended in space but localized in momentum.

From the topological protection exclusive to the  $k_x = 0$  state, one can infer that there will be a robust quantization step in two-terminal conductance measurements while one does not expect any particular quantum Hall signal due to the zero value of the Chern number. We have presented the localization properties of the edge

states and the conductance as a function of the disorder strength for two different kinds of disorder, breaking and preserving the particle-hole symmetry. Our results show that the edge states are quite robust to disorder perturbations, specially if the disorder preserves the particle-hole symmetry. The conductance calculations show indeed the presence of a robust quantization step and the difference between the two types of disorder.

As a final conclusion, our results look deeper into the topological protection of anisotropic 2D materials. Even if the two-dimensional topological number *par excellence*, the Chern number, is zero, the topological properties of the edge states may be non-trivial.

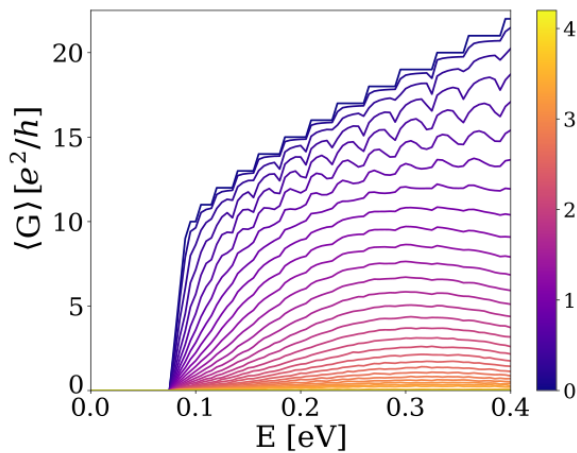


FIG. 9. Conductance for a two-probe nanoribbon with leads in  $y$ -direction and finite width in  $x$ -direction.

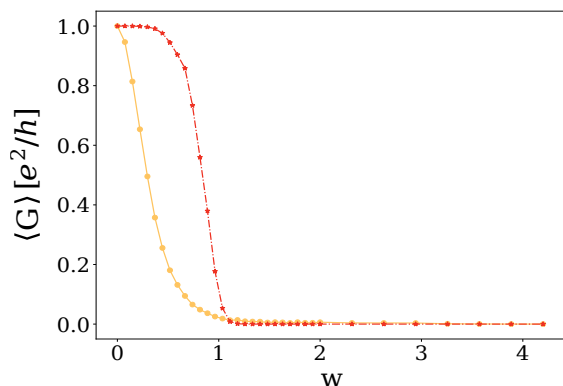


FIG. 10. Averaged conductance in terms of the magnitude of disorder for  $E = 0.04$  eV. The case where the symmetry is preserved, is plotted as a dashed orange line while when the case where the symmetry is broken is represented by a continuous yellow line.

## ACKNOWLEDGMENTS

We acknowledge financial support from the Ministerio de Ciencia e Innovación of Spain (Spanish Ministry of Science, Innovation, and Universities) and FEDER (ERDF: European Regional Development Fund) under Research Grants No. PID2022-136285NB-C31/C32. M.G.O. acknowledges FEDER/Junta de Castilla y León Research Grant No. SA121P20.

- 
- [1] K. S. Novoselov, A. K. Geim, S. V. Morozov, D. Jiang, Y. Zhang, S. V. Dubonos, I. V. Grigorieva, and A. A. Firsov, Electric field effect in atomically thin carbon films, *Science* **306**, 666 (2004).
  - [2] A. H. Castro Neto, F. Guinea, N. M. R. Peres, K. S. Novoselov, and A. K. Geim, The electronic properties of graphene, *Rev. Mod. Phys.* **81**, 109 (2009).
  - [3] M. König, S. Wiedmann, C. Brüne, A. Roth, H. Buhmann, L. W. Molenkamp, X.-L. Qi, and S.-C. Zhang, Quantum spin hall insulator state in hgte quantum wells, *Science* **318**, 766 (2007).
  - [4] X.-L. Qi and S.-C. Zhang, Topological insulators and superconductors, *Rev. Mod. Phys.* **83**, 1057 (2011).
  - [5] J. Maciejko, T. L. Hughes, and S.-C. Zhang, The quantum spin hall effect, *Annual Review of Condensed Matter Physics* **2**, 31 (2011).
  - [6] A. A. Burkov and L. Balents, Weyl semimetal in a topological insulator multilayer, *Phys. Rev. Lett.* **107**, 127205 (2011).
  - [7] Z. K. Liu, B. Zhou, Y. Zhang, Z. J. Wang, H. M. Weng, D. Prabhakaran, S.-K. Mo, Z. X. Shen, Z. Fang, X. Dai, Z. Hussain, and Y. L. Chen, Discovery of a three-dimensional topological dirac semimetal, na 3 bi, *Science* **343**, 864–867 (2014).
  - [8] M. Naumann, F. Arnold, Z. Medvecka, S.-C. Wu, V. Süß, M. Schmidt, B. Yan, N. Huber, L. Worch, M. Wilde, C. Felser, Y. Sun, and E. Hassinger, Weyl nodes close to the fermi energy in nbas, *physica status solidi (b)* **259**, 2100165 (2021).
  - [9] V. Pardo and W. E. Pickett, Half-metallic semi-dirac-point generated by quantum confinement in tio<sub>2</sub>/vo<sub>2</sub> nanostructures, *Phys. Rev. Lett.* **102**, 166803 (2009).
  - [10] S. Katayama, A. Kobayashi, and Y. Suzumura, Electric conductivity of the zero-gap semiconducting state in  $\alpha$ -(BEDT-TTF)<sub>2</sub>I<sub>3</sub> salt, *J. Phys. Soc. Jap.* **75**, 023708 (2006).
  - [11] A. Castellanos-Gomez, L. Vicarelli, E. Prada, J. O. Island, K. L. Narasimha-Acharya, S. I. Blanter, D. J. Groenendijk, M. Buscema, G. A. Steele, J. V. Alvarez, H. W. Zandbergen, J. J. Palacios, and H. S. J. van der Zant, Isolation and characterization of few-layer black phosphorus, *2D Materials* **1**, 025001 (2014).



- [12] A. S. Rodin, A. Carvalho, and A. H. Castro Neto, Strain-induced gap modification in black phosphorus, *Phys. Rev. Lett.* **112**, 176801 (2014).
- [13] G. Liu and X. Lei, Semi-Dirac and Dirac-node-arc phases in a (112) oriented Cd3As2 film, *Journal of Applied Physics* **132**, 224304 (2022).
- [14] W. J. Chan, L. K. Ang, and Y. S. Ang, Quantum transport and shot noise in two-dimensional semi-dirac system, *Applied Physics Letters* (2023).
- [15] G. Montambaux, F. Piéchon, J.-N. Fuchs, and M. O. Goerbig, A universal hamiltonian for motion and merging of dirac points in a two-dimensional crystal, *The European Physical Journal B* **72**, 509 (2009).
- [16] S. S. Banerjee, R. R. P. Singh, V. Pardo, and W. E. Pickett, Tight-binding modeling and low-energy behavior of the semi-dirac point., *Physical review letters* **103** **1**, 016402 (2009).
- [17] G. Montambaux, F. Piéchon, J.-N. Fuchs, and M. O. Goerbig, Merging of dirac points in a two-dimensional crystal, *Phys. Rev. B* **80**, 153412 (2009).
- [18] J. P. Carbotte, K. R. Bryenton, and E. J. Nicol, Optical properties of a semi-dirac material, *Physical Review B* (2019).
- [19] Y. Huang and R. Shen, The generation and detection of the spin-valley-polarization in semi-dirac materials, *Physica Scripta* (2023).
- [20] Z. Zhu, Y. Cheng, and U. Schwingenschlögl, Band inversion mechanism in topological insulators: A guideline for materials design, *Phys. Rev. B* **85**, 235401 (2012).
- [21] S.-Q. Shen, *Topological Insulators*, Springer, Vol. 187 (Springer, 2012).
- [22] D. J. Thouless, M. Kohmoto, M. P. Nightingale, and M. den Nijs, Quantized hall conductance in a two-dimensional periodic potential, *Phys. Rev. Lett.* **49**, 405 (1982).
- [23] C.-X. Liu, S.-C. Zhang, and X.-L. Qi, The quantum anomalous hall effect: Theory and experiment, *Annual Review of Condensed Matter Physics* **7**, 301 (2016).
- [24] H. Huang, Z. Liu, H. Zhang, W. Duan, and D. Vanderbilt, Emergence of a chern-insulating state from a semi-dirac dispersion, *Phys. Rev. B* **92**, 161115 (2015).
- [25] B. Wunsch, F. Guinea, and F. Sols, Dirac-point engineering and topological phase transitions in honeycomb optical lattices, *New Journal of Physics* **10** (2008).
- [26] P. Delplace, D. Ullmo, and G. Montambaux, Zak phase and the existence of edge states in graphene, *Physical Review B* **84**, 10.1103/physrevb.84.195452 (2011).
- [27] J. Zak, Berry's phase for energy bands in solids, *Phys. Rev. Lett.* **62**, 2747 (1989).
- [28] F. Schindler, A. M. Cook, M. G. Vergniory, Z. Wang, S. S. P. Parkin, B. A. Bernevig, and T. Neupert, Higher-order topological insulators, *Science Advances* **4**, eaat0346 (2018), <https://www.science.org/doi/pdf/10.1126/sciadv.aat0346>.
- [29] L. Trifunovic and P. W. Brouwer, Higher-order bulk-boundary correspondence for topological crystalline phases, *Phys. Rev. X* **9**, 011012 (2019).
- [30] C. W. Groth, M. Wimmer, A. R. Akhmerov, and X. Waintal, Kwant: a software package for quantum transport, *New Journal of Physics* **16**, 063065 (2014).
- [31] J. González and R. A. Molina, Topological protection from exceptional points in weyl and nodal-line semimetals, *Phys. Rev. B* **96**, 045437 (2017).
- [32] E. Benito-Matías and R. A. Molina, Surface states in topological semimetal slab geometries, *Phys. Rev. B* **99**, 075304 (2019).
- [33] W. P. Su, J. R. Schrieffer, and A. J. Heeger, Solitons in polyacetylene, *Phys. Rev. Lett.* **42**, 1698 (1979).
- [34] D. Gresch, G. Autès, O. V. Yazyev, M. Troyer, D. Vanderbilt, B. A. Bernevig, and A. A. Soluyanov, Z2pack: Numerical implementation of hybrid wannier centers for identifying topological materials, *Phys. Rev. B* **95**, 075146 (2017).
- [35] P. Delplace, D. Ullmo, and G. Montambaux, Zak phase and the existence of edge states in graphene, *Phys. Rev. B* **84**, 195452 (2011).
- [36] J. K. Asbóth, L. Oroszlány, and A. Pályi, *A Short Course on Topological Insulators* (Springer International Publishing, 2016).
- [37] M. Martí-Sabaté and D. Torrent, Zak's phase in non-symmetric one-dimensional crystals (2021), arXiv:2107.10144 [cond-mat.mtrl-sci].
- [38] S. Ryu and Y. Hatsugai, Topological origin of zero-energy edge states in particle-hole symmetric systems, *Physical Review Letters* **89**, 10.1103/physrevlett.89.077002 (2002).
- [39] S. Datta, *Electronic transport in mesoscopic systems* (1995).
- [40] B. Zhou, H.-Z. Lu, R.-L. Chu, S.-Q. Shen, and Q. Niu, Finite size effects of helical edge states in hgte/cdte quantum wells (2008).

## Appendix A: Edge states

This appendix details the calculations involved in analytically deriving the dispersion relation of the edge states (6). We follow the procedure of Ref. [40] considering a nanoribbon finite in  $y$ -direction and periodic boundary conditions in  $x$ -direction. In this scenario,  $k_x$  is a good quantum number and  $k_y$  is replaced by Peierls substitution  $k_y \rightarrow -i\partial_y$ . For simplicity, we consider each edge separately, treating them as isolated edges of the infinite half-planes defined by  $y \geq W/2$  for the upper edge and  $y \leq -W/2$  for the lower edge. We choose these limits instead of  $y > 0$  and  $y < 0$  by analogy with the numerical implementation of the system. As previously mentioned, we choose wave functions that vanish at the edges, for  $y = \pm W/2$ , and decays towards the bulk with decay length  $\lambda$ . This decay behavior is captured by assuming a spatial dependence of the wave function of the form  $\psi_{k_x}^{\pm} \sim e^{ik_x x} e^{\mp\lambda(\pm W/2 - y)} (\alpha \beta)^T$ . Introducing this ansatz into the Schrödinger equation yields to the following dispersion relation

$$E = \pm \sqrt{[M_0 - M_1(k_x^2 - \lambda^2)]^2 + V_x^2 k_x^4 - V_y^2 \lambda^2}, \quad (\text{A1})$$

where, here,  $+$  refers to the upper band and  $-$  refers to the lower band, equal for both edges. By reversing this expression, we obtain four possible solutions for  $\pm\lambda_1$  and  $\pm\lambda_2$ ,

$$\lambda_i = \sqrt{k_x^2 + \frac{V_y^2 - 2M_0M_1}{2M_1^2} \pm \frac{\sqrt{V_y^4 + 4M_1^2(k_x^2V_y^2 - V_y^2M_0/M_1 - V_x^2k_x^4 + E^2)}}{2M_1^2}}, \quad i = 1, 2. \quad (\text{A2})$$

Thus, in order to ensure a proper decay, ( $\text{Re}(\lambda) > 0$ ), the positive values of  $\lambda$  describe edge states decaying from the upper edge while negative values of  $\lambda$  describe edge states decaying from the lower edge. The solutions has a general form,

$$\psi_{k_x}^{\pm} \sim A_1 \begin{pmatrix} \alpha_1 \\ \beta_1 \end{pmatrix} e^{\mp\lambda_1(\pm W/2 - y)} + A_2 \begin{pmatrix} \alpha_2 \\ \beta_2 \end{pmatrix} e^{\mp\lambda_2(\pm W/2 - y)}. \quad E^{\pm} = M_0 - M_1(k_x^2 - \lambda_1\lambda_2) \mp M_1 \frac{V_x}{V_y} k_x^2 (\lambda_1 + \lambda_2). \quad (\text{A3}) \quad (\text{A7})$$

where, here, + in for the upper edge and - for the lower one. The Dirichlet boundary conditions  $\psi_{k_x}^{\pm}(y = \pm W/2) = 0$  provides the following relation

$$\alpha_1\beta_2 - \beta_2\alpha_1 = 0 \quad (\text{A4})$$

Then, by introducing this general solution in the Schrödinger equation, we can get a relation between these coefficients and the parameters of the model

$$\alpha_i^{\pm} = V_x k_x^2 \mp V_y \lambda_i; \quad (\text{A5})$$

$$\beta_i = E - M_0 + M_1(k_x^2 - \lambda_i^2) \quad (\text{A6})$$

By combining (A4) and (A5) we obtain the dispersion relation of the edge states in terms of the decay lengths,

Now, we perform an expansion around  $k_x = 0$ , to obtain the final expression

$$E^{\pm} = M_0 - M_1(\lambda_1^{(0)}\lambda_2^{(0)}) \pm M_1 \frac{V_x}{V_y} (\lambda_1^{(0)} + \lambda_2^{(0)}), \quad (\text{A8})$$

where  $\lambda_i^{(0)}$  refers to decay lengths evaluate in  $k_x = 0$ . For the derivatives we have take into account that

$$\left. \frac{d\lambda_i}{dk_x} = \frac{1}{\lambda_i} \left[ 2k_x \mp \frac{8M_1^2(k_x V_y^2 - 2k_x^3 V_x^2)}{\sqrt{V_y^4 + 4M_1^2(E^2 - k_x^4 V_x^2 + k_x^2 V_y^2 - V_y^2 M_0/M_1)}} \right] \right|_{k_x=0} = 0 \quad (\text{A9})$$

$$\lambda_1\lambda_2 = \sqrt{Q + R}; \quad \left. \frac{d\lambda_1\lambda_2}{dk_x} \right|_{k_x=0} = 0, \quad \left. \frac{d^2\lambda_1\lambda_2}{dk_x^2} \right|_{k_x=0} = -2 \quad (\text{A10})$$

$$Q = k_x^4 + k_x^2 \frac{V_y^2 - 2M_0M_1}{M_1^2} \frac{(V_y^2 - 2M_0M_1)^2}{4M_1^4} \quad (\text{A11})$$

$$R = \frac{1}{4M_1^4} \left[ V_y^4 + 4M_1^2 \left( E^2 + k_x^2 V_y^2 - k_x^4 V_x^2 - V_y^2 M_0/M_1 \right) \right]$$